

Chapter 36

Failure Processes Governing High Rate Impact Resistance of Epoxy Resins Filled with Core Shell Rubber Nanoparticles

Erich D. Bain, Daniel B. Knorr Jr., Adam D. Richardson, Kevin A. Masser, Jian Yu, and Joseph L. Lenhart

Abstract Epoxy resins are classically toughened by rubber additives, but the effectiveness of rubber toughening tends to diminish with increasing strain rate, decreasing temperature, and decreasing matrix ductility. In this study we demonstrate that low loadings of 100–200 nm core-shell rubber (CSR) particulate additives can improve high strain rate (10^4 – 10^5 s⁻¹) impact resistance by nearly 200 % for epoxy resins with glass transition temperatures T_g in a range between 60 and 110 °C, without large reductions in T_g or stiffness. Size and surface chemistry of the CSR particles influence the ballistic response, with 200 nm diameter, weakly bound, poorly dispersed CSR particles providing the greatest toughening performance at low filler loadings and high rates. Impact resistance for a systematic series of CSR modified epoxies covers a transition from brittle to tough behavior, where the failure mechanism changes with effective fracture resistance. For brittle resins, failure is dominated by initiation of Hertzian cone fracture which depends strongly on fracture toughness K_{IC} , while for tough resins, failure is dominated by plastic yield at the impact site and is independent of fracture toughness above a minimum K_{IC} value of approximately 1.2–1.5 MPa·m^{1/2}. Interestingly, quasistatic mechanical properties are reasonably effective qualitative predictors of high rate impact resistance, suggesting that the toughening mechanisms of CSR particles are similar over the rates studied here. The insights gained from this study are valuable for design of next generation adhesives, polymers, and polymer composite matrices for lightweight protective applications.

Keywords Rubber toughened epoxies • High rate impact resistance • Failure mechanisms • Composites • Fracture

36.1 Introduction

Cross-linked epoxy polymers are major components in technologically important material packages such as fiber reinforced polymer composites (FRPCs), adhesives, coatings, and bulk plaques for protective systems servicing a wide range of military, aerospace, transportation, and construction industries [1–3]. In FRPCs, where epoxy resin acts as the matrix, the relationship between epoxy toughness and composite high rate impact resistance is complex. Tensile failure of primary yarns and interlaminar delamination tend to be two primary dissipative mechanisms, where the former is dominated by the fiber properties [4], while the latter is at least partially dependent on the matrix [5]. For example, Kinloch, Sprenger, and coworkers have shown that interlaminar fracture energy G_c for a range of fiber and weave types systematically increases with epoxy matrix fracture toughness, when the matrix is toughened with rubbery particles, silica nanoparticles, or both [6, 7]. These authors additionally demonstrated improved high rate impact resistance of carbon fiber composites formulated with a “hybrid” epoxy matrix containing both rubber and silica toughening particles [7]. While optimization of fibers and laminates is well advanced [8], less work has been done to understand and optimize high rate impact resistance of the epoxy matrix itself [9–12].

Extensive research has focused on improving fracture toughness of epoxies through hard and soft particulate additives [13–19], as well as the manipulation of the epoxy chemistry and chain structure [20, 21]. Rubber toughening is a common approach for improving the quasi-static fracture toughness in epoxy thermosets [22, 23], and is capable of improving fracture resistance by a factor of 2 or more through incorporation of phase-separated liquid rubber particles [13–15, 24, 25], block copolymer micelles [26–29], or pre-formed core-shell rubber (CSR) particles [19, 30–32]. A primary mechanism of thermoset toughening by particulate fillers is particle cavitation or debonding of the matrix from the particles, both of which relieve the triaxial constraint ahead of a propagating crack and initiate plastic void growth and shear band formation in

E.D. Bain (✉) • D.B. Knorr Jr. • A.D. Richardson • K.A. Masser • J. Yu • J.L. Lenhart
U.S. Army Research Laboratory, 4600 Deer Creek Loop, Aberdeen Proving Ground, Aberdeen, MD 21005, USA
e-mail: erich.d.bain.civ@mail.mil

matrix ligaments between voids [24, 33, 34]. However, particle cavitation does not guarantee the beginning of matrix shear deformation, but must produce a stress concentration sufficiently close to the matrix yield stress to induce local shear deformation, making the shear strength (i.e., ductility) of the matrix an important parameter [19, 35].

More ductile resins are generally more effectively toughened at quasistatic rates via the matrix void growth and matrix shear banding mechanism described above, with the molecular weight between crosslinks (M_c) being a predictor of toughenability [25, 36]. This has resulted in poor additive toughening of highly crosslinked materials over a wide temperature range relative to glass transition temperature T_g , while readily toughenable resins have showed improved properties even far below T_g [37]. Furthermore, while quasi-static fracture has been intensively investigated, high rate performance is less well understood. The effectiveness of rubber toughening tends to decrease as strain rate increases or temperature decreases [14, 15, 27, 38, 39]. Therefore, a key question for protection applications is, “Does rubber toughening work at ballistic impact strain rates over the broad temperature ranges required for practical applications?”

Our previous work [10–12] has shown that improvements in ballistic performance of crosslinked polymer networks tend to come at the expense of reductions in modulus and/or T_g , which are undesirable for many structural applications. Therefore, the present work [40] is motivated by a need to improve high strain rate impact resistance within an epoxy matrix, over a broad range of operational temperatures, while simultaneously maintaining a relatively high glass transition temperature and glassy modulus. Our model system is composed of low loadings of core-shell rubber (CSR) nanoparticles integrated into diamine cured DGEBA resins, which exhibit a broad range of glass transition temperatures. The epoxy used in this study, DGEBA, is commonly found in many applications, and the T_g and M_c of the network were tuned by varying the diamine hardener.

36.2 Experimental

All materials used in this experiment were purchased from Sigma-Aldrich unless noted otherwise. Diglycidyl ether of bisphenol A (DGEBA) was purchased from Hexion Inc. under the product name EPON 825. PACM (4,4'-methylenebis(cyclohexylamine)) was purchased from Air Products. Samples of polyetheramines, trademarked as Jeffamine D-230 and D-400, were supplied by Huntsman Chemical. Kane Ace MX-125, MX-156, and MX-257 are core-shell rubber (CSR) particle formulations pre-dispersed in DGEBA, and were provided by Kaneka, USA. A listing of the CSR particle characteristics is given in Table 36.1. MX-125 and MX-156 contain a small percentage of epoxy groups in the PMMA shell, while MX-257 has no epoxy or other reactive groups in the PMMA shell. The chemical structures of all monomers used are given in Fig. 36.1. As all samples contain DGEBA, they will be referred to throughout the paper by the amine hardener and what weight percent, if any, of CSR they contain.

The preparation for both quasistatic and high rate specimens was identical. Stoichiometric amounts of epoxy (with the desired amount of CSR filler) and diamine were heated to 60 °C. They were then mixed using an overhead mixer for 5 min. The mixture was degassed, poured into stainless steel molds (6 in. × 6 in. × 0.25 in.) that had been polished, treated with Frekote 55NC release agent, and pre-heated to 60 °C, and degassed once more. All formulations were cured under a nitrogen purge with a cure cycle of 80 °C for 2 h, 150 °C for 8 h, 200 °C for 2 h.

Ballistic tests [41] were carried out using a 0.22 caliber gas gun. The projectile was a 5.56 mm diameter stainless steel ball bearing (Type 302, 0.69 g) and its speed was measured by Doppler radar (BR-3502, Infinition Inc.). The polymer specimen dimensions were 62.5 mm × 62.5 mm × 6.4 mm. Each specimen was sandwiched between two aluminum plates with a 50.8 mm diameter circular aperture. An aluminum foil witness plate (0.0108 mm thick) was placed 50.8 mm behind the target. Ballistic failure of the epoxy was assigned when the projectile or a fragment of the epoxy target penetrated the witness

Table 36.1 MX series core-shell rubber (CSR) nanoparticle properties

Product	Loading in DGEBA (%wt)	Nominal particle size (nm)	Measured particle size (nm) ^a	Core composition	Core T_g (°C) ^b	Shell composition	Shell functionalization
MX-125	25	100	104 ± 10	PS/PB	−50	PMMA	Some epoxy
MX-156	25	100	104 ± 7	PB	−75	PMMA	Some epoxy
MX-257	37	200	167 ± 8	PB	−71	PMMA	None

^aNumber average diameters measured from SEM images of as-received particle mixtures spincast from toluene and cured with PACM

^bTaken from low temperature peaks in DMA tan δ curves of particle mixtures cured with D230

Fig. 36.1 Structures of epoxy (DGEBA) and diamine curing agents used in this study

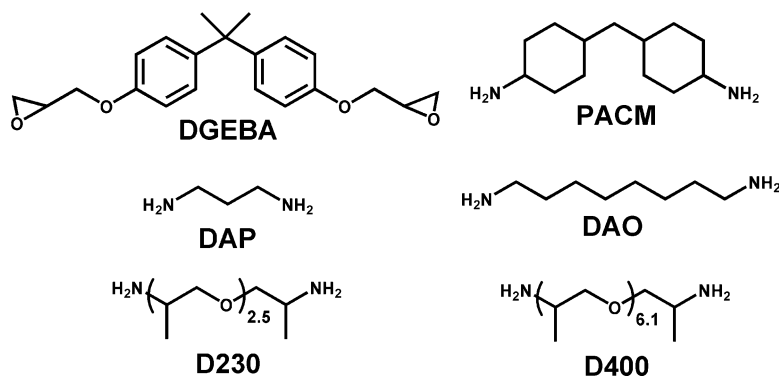


plate. Twelve targets were used of each formulation. The V_{50} ballistic limit was calculated by taking the arithmetic mean of the three highest non-failed and the three lowest failed impact velocities. The kinetic energy associated with V_{50} , i.e., KE_{50} , was obtained from the V_{50} value and the mass of the projectile m , as $KE_{50} = 0.5 mV_{50}^2$. Selected impact events were imaged at 180,000 frames per second using a FASTCAM SA1.1 model 675 K-M1 high speed video camera (Photron USA, Inc.) mounted behind the specimen back face, with specimens illuminated from the front.

Dynamic mechanical analysis (DMA) was conducted to determine T_g using a TA Instruments Q800 on samples that were nominally 35 mm × 12 mm × 3.25 mm for the rubbery region and 35 mm × 12 mm × 1.5 mm for the glassy region. The quasistatic mode I fracture toughness of epoxy resins was determined according to ASTM D5045-99 using the single-edge-notch bending (SENB) geometry with dimensions of 6.35 mm × 12.7 mm × 63 mm ($B \times W \times L$) and a cross head speed of 10 mm/min. The pre-crack was initiated by tapping with a cryogenically frozen razorblade. Tensile specimens were molded to the dimensions of ASTM D638-10, Type IV. Cross head speed was 5 mm/min and digital image correlation (DIC) was used to obtain strain values. Compression samples 12 mm in diameter and 6 mm thick were prepared and tested using ASTM D695-10 as a guide, with cross head speed of 1.3 mm/min. Selected fracture surfaces of tested specimens were sputtered with an approximately 5 nm thick film of gold-palladium and were imaged in a Hitachi S-4700 scanning electron microscope using an accelerating voltage of 3 kV.

36.3 Results and Discussion

36.3.1 Effect of CSR Particles on Ballistic and Quasistatic Performance as a Function of Glass Transition Temperature

We produced a series of DGEBA resins cured with the diamine hardeners shown in Fig. 36.1, both neat and filled with MX-125 such that the overall CSR nanoparticle concentrations are 1, 3, and 5 wt%. Results of ballistic impact tests for this series of resins are plotted in Fig. 36.2 in the form of KE_{50} , the projectile kinetic energy associated with a 50 % probability of target failure, as a function of $T - T_g$, where T is the measurement temperature of 22 °C. For clarity, the results are normalized using the KE_{50} value of unfilled PACM/DGEBA as a standard. The “x” symbols shown in Fig. 36.2 represent data for previously studied [10] diamine cured DGEBA resins measured at 22 °C without any rubber fillers, to provide context for the present measurements. The step change in KE_{50} values for unmodified resins at about 25 °C below T_g is similar to that observed for other materials such as polyurethane coatings [42–45].

T_g values of all resins (measured by DMA) do not change significantly upon addition of the CSR particles. KE_{50} values of the highest T_g resins, including those cured with PACM, DAP, and DAO, do not show significant improvement with CSR nanoparticle modification up to 5 wt% over the relatively poor performance of the unfilled resins. In contrast, KE_{50} of DGEBA cured with D230 more than doubles for the resins filled with 3 and 5 wt% nanoparticles, while the 1 wt% sample shows a modest improvement. Interestingly, the modified D400 cured resin does not show significant improvement over the already high normalized KE_{50} value of about 3.5.

Although mode I fracture toughness is not strictly analogous to impact resistance, the two quantities can be related via the complex set of fracture processes involved in impact failure [46–48]. In Fig. 36.3 we compare literature values of quasistatic mode I fracture toughness (K_{IC}) for various epoxies cured with different monomers and diamine hardeners, covering a wide range of $T - T_g$ values, next to quasistatic K_{IC} values measured for the neat and CSR-modified samples in this study. The

Fig. 36.2 Normalized high rate impact resistance KE_{50} of MX-125 core-shell rubber modified DGEBA cured with various diamines as a function of $T-T_g$: PACM (filled square), DAP (filled circle), DAO (filled up-pointing triangle), D-230 (filled down-pointing triangle), and D-400 (filled diamond). Previous data for unfilled resins from [10] are represented by (x). The dotted line is intended as a guide to the eye for the trend in KE_{50} of the unfilled resins

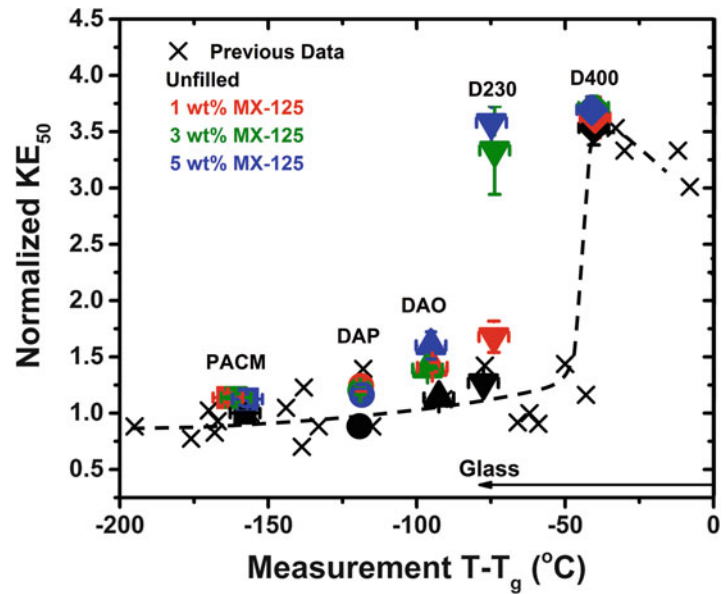
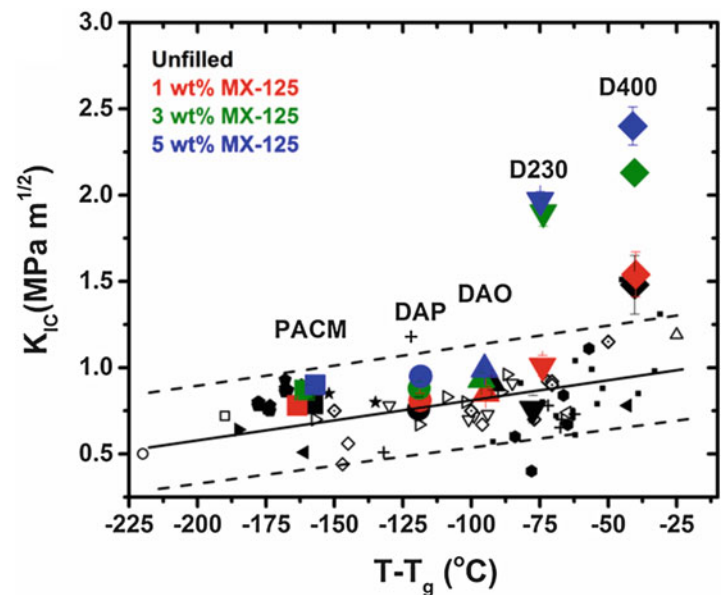


Fig. 36.3 Quasistatic fracture toughness K_{IC} as a function of $T-T_g$ for CSR-modified epoxies (large symbols same as Fig. 36.2). Small black symbols represent unmodified epoxy/diamine systems from the literature [40]. The solid line is a guide for the eye illustrating the approximate trend in the literature data, while the dotted lines encompasses ~95 % of the data



results agree well with general trends in the literature, showing that matrix toughenability due to rubber additives tends to increase with increasing $T-T_g$ [19, 28, 29]. Higher T_g resins including PACM, DAP, and DAO cured DGEBA exhibit little toughening effect in quasistatic K_{IC} as a result of CSR addition. D230 shows a minimal toughening effect at 1 wt% but a high degree of toughening at 3 wt% and 5 wt% modifier, reminiscent of the trends observed for KE_{50} of this resin. However, quasistatic K_{IC} of D400 also increases dramatically with increasing loading of CSR particles, in contrast to the negligible effect caused by the same filler on KE_{50} of this resin.

36.3.2 Effect of CSR Particle Size and Surface Functionality on Ballistic and Quasistatic Performance of DGEBA-D230 Resin

Because the DGEBA/D230 system exhibits large increases in both quasistatic fracture toughness and ballistic impact resistance with the addition of MX-125, we have investigated this resin further with additional CSR nanoparticle types.

These particle types include MX-156, which is similar to MX-125 in size (nominally 100 nm) and shell functionality (lightly epoxidized), but whose polybutadiene core has a lower T_g than the polystyrene-butadiene core of MX-125, and MX-257, which is larger (nominally 200 nm) and features an unfunctionalized PMMA shell and soft polybutadiene core. These attributes are summarized in Table 36.1.

Normalized room temperature KE_{50} data for DGEBA/D230 modified with each of the three CSR nanoparticle types is shown as a function of particle loading in Fig. 36.4. The performance of the two 100 nm particle additives (MX-125 and MX-156) is very similar: KE_{50} increases with loading up to 3 wt%, where a plateau KE_{50} value of about 3.5 is reached. In the case of D230 modified with the larger MX-257 particles, a similar plateau in KE_{50} is reached but for loadings as low as 0.5 wt%, suggesting that either particle size, surface functionalization, or both play important roles in the impact resistance.

Quasistatic fracture toughness K_{IC} of D230 as a function of filler loading for the three CSR particle types are shown in Fig. 36.5. The effects of MX-125 and MX-156 are similar over most of the loading range, reaching a plateau in quasistatic K_{IC} at a loading of about 5 wt%. The behavior of D230 containing MX-257 particles follows a similar trend, with slightly higher K_{IC} values. Unlike KE_{50} , which increase sharply at loadings of about 2 wt% for MX-125 and MX-156 and 0.5 wt% for MX-257, the increase in quasistatic fracture toughness with loading is more gradual for all three particle types.

Fig. 36.4 Normalized high rate impact resistance KE_{50} as a function of CSR nanoparticle content for modified DGEBA/D230. The dotted lines are intended as guides for the eye

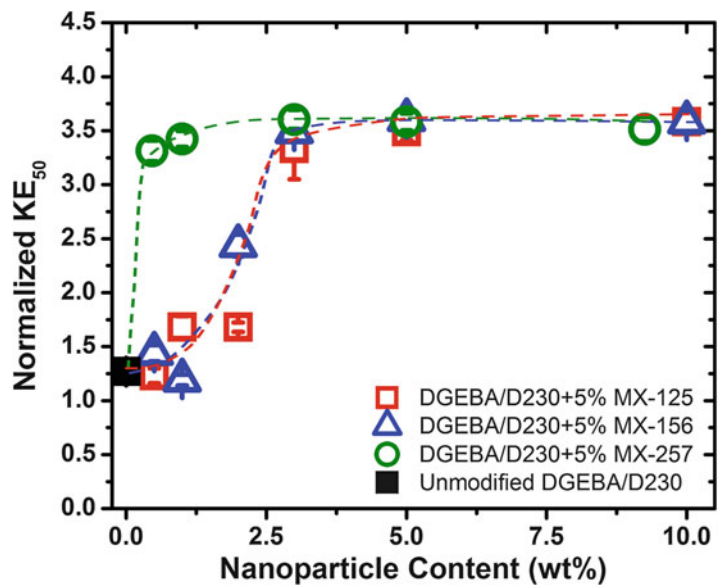
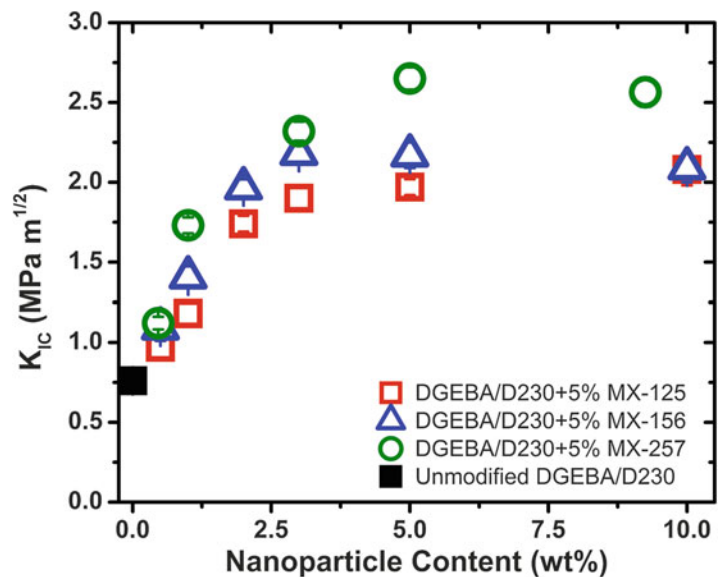


Fig. 36.5 Quasistatic fracture toughness K_{IC} as a function of CSR nanoparticle content for modified DGEBA/D230



36.3.3 Damage Types Associated with Ballistic Impact

In order to better understand the complex relationship between high rate impact resistance and mode I fracture toughness, it is necessary to understand the sequence of failure processes involved in ballistic impact events and the governing parameters for each type of damage. Photographs and schematics illustrating various damage types in ballistically impacted epoxy plates are shown in Fig. 36.6. Three types of ballistic damage will be considered in our treatment: radial cracking, cone cracking, and plastic deformation at the impact site.

Upon impact with steel spheres during V_{50} tests, all materials in this study formed radial cracks similar to those shown in Fig. 36.6a, b. Radial cracks are known to initiate at the target back face due to bending stress ahead of the impact site [46, 49]. In this study neat and modified epoxy tiles impacted at velocities well below the failure velocity V_{50} tended to form radial cracks only, whereas targets impacted at higher velocities formed both radial cracks and cone cracks. Radial cracks tended to originate from the $r = 0$ point immediately ahead of the impact site on the back face, propagating toward the sample edges and passing smoothly through the orthogonal cone cracks, if present, as seen for example in Fig. 36.6b. From these observations we hypothesize that radial cracks initiate prior to cone crack initiation, consistent with predictions for targets whose thickness is on the order of the projectile diameter [46, 50]. Furthermore, these observations suggest that radial cracking is a necessary, but not sufficient condition for target failure according to the V_{50} test.

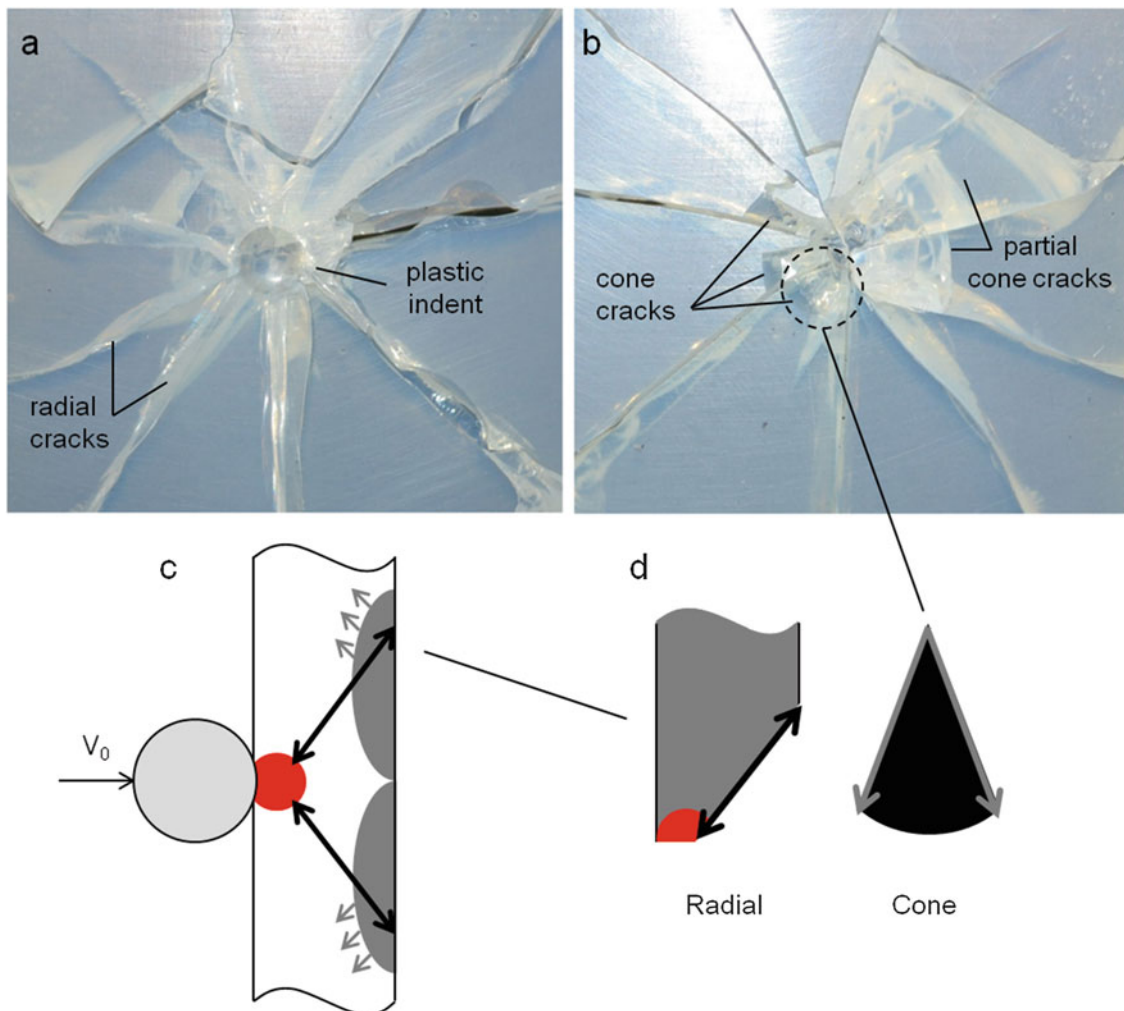


Fig. 36.6 (a) Front face of ballistically impacted DGEBA-D230 containing 5 wt% MX-125 CSR particles, showing plastic indentation from projectile and radial cracks. (b) Back face of same specimen showing cone cracks and radial cracks. (c) Schematic illustrating damage types during ballistic impact: plastic zone (red), cone cracks (black), and radial cracks (gray). (d) Schematic of fracture surface sections taken for SEM imaging

If the stress intensity at a flaw near the impact site exceeds the fracture toughness K_{IC} of the target, a ring crack will initiate. This crack tends to propagate along a cone-shaped trajectory opening from the front face toward the back. For ideally elastic (Hertzian) contact, the critical impact velocity for cone crack initiation V_c can be estimated from analytical relationships [46, 48]:

$$V_c \approx \frac{950K_{IC}^{5/3}}{R\rho_1^{1/2}E^{*7/6}} \quad (36.1)$$

where K_{IC} is the fracture toughness of the target, R is the projectile diameter, ρ_1 is the projectile density, E^* is a reduced contact modulus [46], and the subscripts 1 and 2 designate the projectile and target, respectively.

The specimen shown in Fig. 36.6a features a circular indentation at the impact point on the front face, indicative of plastic deformation. Similar plastic indentations were observed for all targets with normalized KE_{50} between 3 and 4, whereas the most brittle targets with low ballistic limits had little or no indentation when impacted at V_{50} . Compton et al. [46] have used finite element simulations and experiments to investigate the critical velocity for plastic deformation (yielding) of ceramic tiles impacted with metal spheres. For projectiles in a high velocity regime, yield initiation was found to follow

$$V_Y \approx \frac{3\sigma_{Y,2}}{(\rho c)'} \quad (36.2)$$

Where $\sigma_{Y,2}$ is the yield stress of the target and $(\rho c)'$ is a reduced acoustic impedance of contact [46]. It is important to note that Eq. (36.2) was derived from simulation results for ceramic targets, whose yield stress is 5–10 times that of the metal projectile. In that case, the projectile deforms plastically prior to target yielding at intermediate and high velocities, causing significant deviations from the ideal Hertzian contact radius and pressure distribution. In our system, deviations from Hertzian contact also occur at high velocities, but it is due solely to plastic deformation of the epoxy targets, whose yield stresses are an order of magnitude lower than that of the steel projectile. Hence, Eq. (36.2) may not quantitatively describe the yield initiation threshold of our system. However, qualitative insight from Eq. (36.2) is valuable, and an essential prediction of these equations is that the critical velocity for yield initiation is a relatively simple function of target yield stress.

36.3.4 High Speed Videography of Ballistic Failure Events

Failure processes occurring during ballistic impact of selected specimens were imaged by a high speed video camera at 180,000 frames per second, as shown in Fig. 36.7. These images demonstrate that radial and cone cracks initiate within 10's

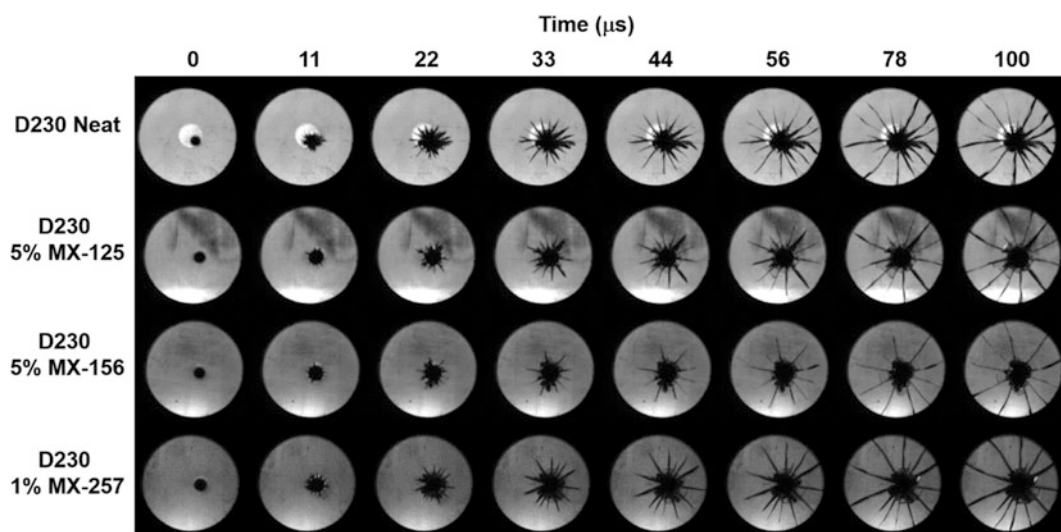


Fig. 36.7 High-speed camera images taken from the back face of samples impacted near V_{50} , including neat D230 (top row) and D230 containing 5 wt% MX-125 (row 2), 5 wt% MX-156 (row 3), and 1 wt% MX-257 (row 4), arranged as a function of time

of microseconds following impact, suggesting minimal time is available for plastic deformation processes associated with rubber toughening. These images provide visual evidence that radial cracks initiate prior to cone cracks during high rate impact. Material sections formed by cone cracks ahead of the impact site were observed to eject from samples at relatively long times (>2 ms, images not shown) and penetrate the witness foil, implying that cone cracking is a primary mechanism of specimen failure according to the standard V_{50} test for the materials in this study.

36.3.5 Fracture Surface Analysis of DGEBA-D230 Modified with Various CSR Particle Types

We now turn our focus to morphological evidence for the role played by the CSR additives in the failure processes described above, using scanning electron microscopy (SEM) images of filled and unfilled D230 fracture surfaces.

SEM images at high magnification of quasistatic K_{IC} process zones in rubber-modified DGEBA-D230 are shown in the top row of Fig. 36.8. Detailed analysis of void sizes formed on these fracture surfaces [40], suggest that MX-125 and MX-156 CSR particles form voids via cavitation of the rubber cores. On the other hand, results suggest voids around MX-257 particles are formed via matrix debonding around weakly bonded particles, rather than solely cavitation of the particle cores. Both of these void formation mechanisms are consistent with classical rubber toughening via plastic void growth and shear banding [24, 33]. The thermodynamically unfavorable particle-matrix interface causes MX-257 to form aggregates of 5–10 particles during curing, whereas MX-125 and MX-156 particles are well dispersed in the D230 matrix. Greater toughening effectiveness of aggregated, weakly bonded rubber particles has been previously observed due to an apparent tendency to depress yield stress and increase the size of the crack-tip plastic zone [31, 51]. Bright lines on the MX-257 filled fracture surface display clear evidence of significant matrix plastic deformation, consistent with high fracture resistance. Neat D230 shows no evidence of deformation or toughening mechanisms in high magnification SEMs [40].

The second row of Fig. 36.8 shows the unstable crack propagation regions (far ahead of the precrack tip [40]) of the quasistatic K_{IC} fracture surfaces. In this region of MX-125 and MX-156 filled systems there is little evidence of particle cavitation or matrix plastic deformation, consistent with rapid, unstable propagation of the crack front after reaching K_{IC} . On the other hand, the unstable fracture region of MX-257 filled D230 features matrix-particle debonding as well as lines indicating matrix deformation. These results suggesting that the toughening effect of MX-257 may be less rate-sensitive than those of MX-125 and MX-156, since crack propagation is known to speed up after becoming unstable.

The third row of high magnification SEM images in Fig. 36.8 are taken from cone crack surfaces near the ballistic impact sites. The fourth row of Fig. 36.8 contains SEM images taken near the back face on the same cone cracks. Particle morphologies on these cone cracks are similar to those seen in unstable fracture regions of quasistatic K_{IC} samples (row 2), but with a greater degree of contrast in the interior of MX-125 and MX-156 particles, suggesting the particle cores have cavitated to form shallow voids. Voids around MX-257 particles are similar to or slightly smaller than those in the unstable fracture region of quasistatic K_{IC} test, but lines indicating significant matrix plastic deformation appear, similar to those observed on the quasistatic crack surfaces.

No regions of greater average void diameter, analogous to process zones observed for quasistatic K_{IC} samples, could be found on any ballistic fracture surface specimens, including near the impact site. The reason for the lack of observed process zones is likely due to the time available for stable crack growth; in quasistatic K_{IC} tests the process zone develops over a period of 1–4 s, during which load increases steadily as a function of displacement until K_{IC} is met and unstable fracture begins. Conversely, as shown in Fig. 36.7, in the KE_{50} test radial and cone cracks initiate and propagate on the order of microseconds. Therefore any corresponding process zone would be vanishingly small due to the extremely limited time available for stable crack growth, as well as for cavitation/debonding and matrix plastic deformation processes. Since no observable process zone is formed, the toughening mechanism of CSR particles during high rate impact cannot be determined from these results. Two reasonable hypotheses are that (1) CSR particles do resist crack initiation during the initial microseconds of high rate impact via stable fracture, in which void formation and matrix plastic deformation occur in a small process zone that may be lost or destroyed during subsequent failure processes such as spallation, or (2) CSR particles continuously resist crack growth via a limited extent of void formation and matrix plastic deformation over the entire course of crack propagation [40].

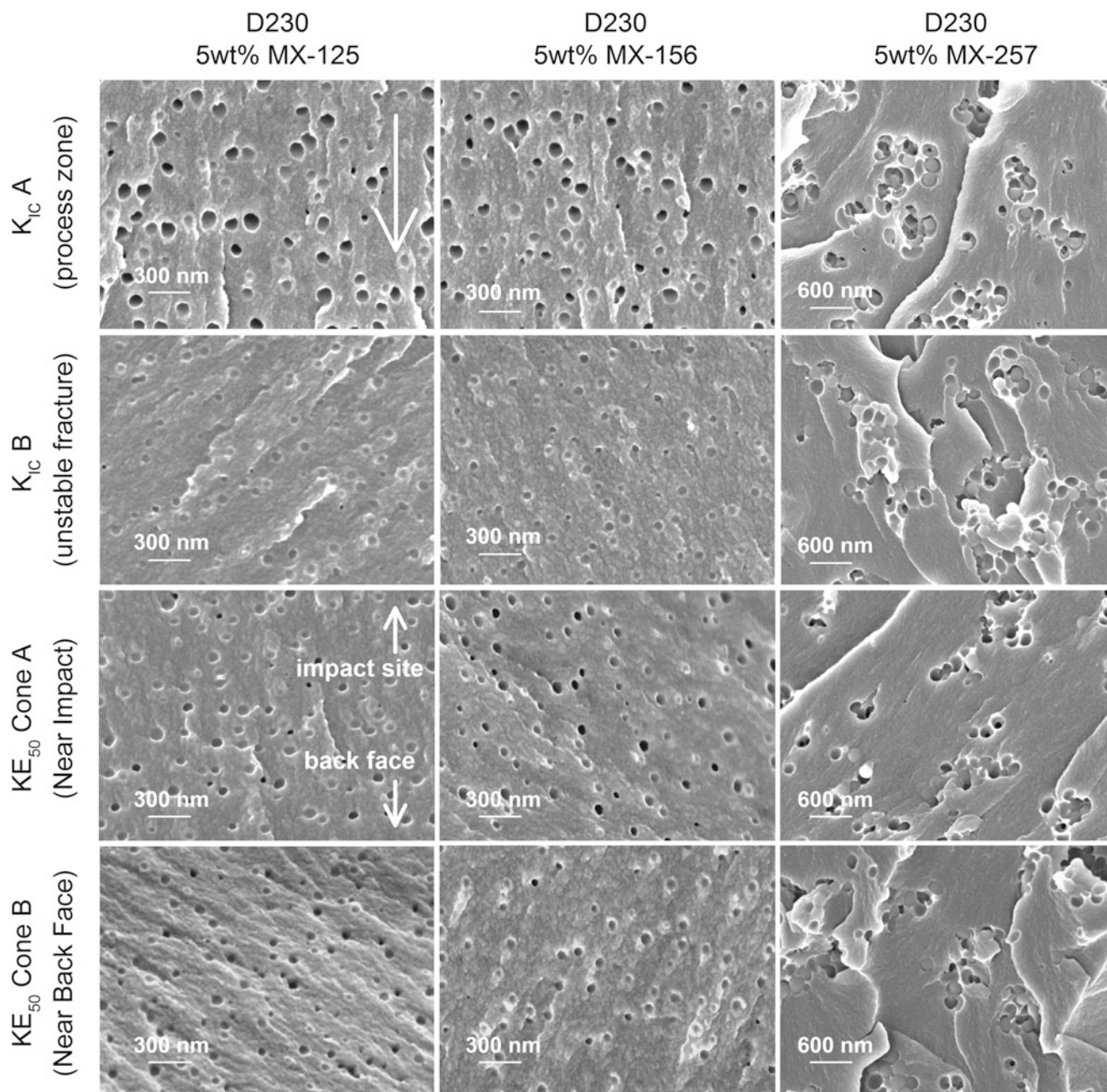


Fig. 36.8 High magnification scanning electron microscopy (SEM) images including fracture surfaces of DGEBA-D230 modified with 5 wt% each of MX-125 (left column), MX-156 (center column), and MX-257 (right column). Process zone (row 1) and unstable fracture (row 2) images are from quasistatic K_{IC} fracture surfaces. Near impact (row 3) and near back face (row 4) images are from ballistic KE_{50} cone crack surfaces. Arrows indicate the direction of crack propagation for K_{IC} images, and the orientation relative to impact site and back face for cone crack images

36.3.6 Correlations Between Quasistatic and Ballistic Performance

Given the preceding investigations of impact failure processes and fracture surface morphology, we are now in a better position to understand the relationships between ballistic impact resistance and quasistatic mechanical properties of the rubber toughened epoxies. To this end, Fig. 36.9 shows a plot of KE_{50} measurements from Figs. 36.2 to 36.4 as a function of quasistatic K_{IC} measurements from Figs. 36.3 to 36.5. Plotted in this way, most of the data fall into two groups: brittle resins with $K_{IC} \leq 1 \text{ MPa}\cdot\text{m}^{1/2}$ and $KE_{50} < 2$, and tough resins with $K_{IC} > 1 \text{ MPa}\cdot\text{m}^{1/2}$ and $KE_{50} \approx 3.5$. The red dashed curve in Fig. 36.9 is a least squares fit of Eq. 36.1 using different values of Young's modulus for selected filled and unfilled resins

Fig. 36.9 Plot of KE_{50} as a function of quasistatic K_{IC} using all data from Figs. 36.2 to 36.5. Closed symbols represent unmodified resins while open symbols correspond to resins modified with CSR particles, with symbol shapes indicated in the legend. The lines are best fits to Eqs. (36.1) (red dotted line) and 36.3 (blue dashed line), using experimental values of Young's modulus and yield stress from quasistatic tensile tests, summarized in Table 36.2

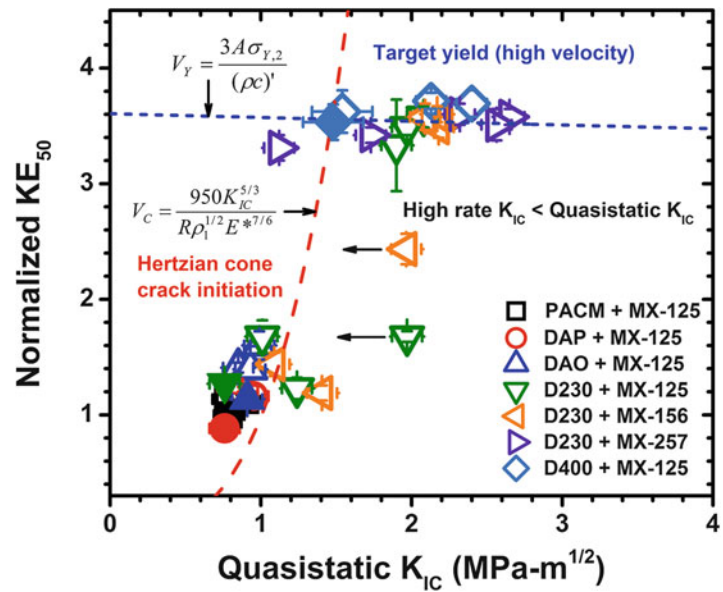


Table 36.2 Quasistatic mechanical properties measured for selected filled and unfilled DGEBA resins at room temperature

Diamine	Modifier	Young's modulus (MPa)	Tensile yield stress (MPa)	Compressive yield stress (MPa)	K_{IC} ($\text{MPa}\cdot\text{m}^{1/2}$)	G_{IC} (J/m^2)	Ballistic failure type
PACM	None	2180 ± 140	–	116 ± 3	0.8 ± 0.1	240 ± 20	Brittle
DAP	None	2510 ± 70	–	106 ± 1	0.8 ± 0.1	240 ± 50	Brittle
DAO	None	2000 ± 50	–	81 ± 1	0.9 ± 0.1	390 ± 30	Brittle
D230	None	3070 ± 140	70 ± 5	87 ± 1	0.8 ± 0.1	180 ± 30	Brittle
D230	1 wt% MX-125	3010 ± 260	66 ± 1	84 ± 1	1.0 ± 0.1	430 ± 60	Brittle
D230	5 wt% MX-125	2830 ± 160	59 ± 1	79 ± 1	2.0 ± 0.1	1530 ± 150	Tough
D230	1 wt% MX-156	2970 ± 120	67 ± 1	83 ± 1	1.4 ± 0.1	580 ± 100	Mixed
D230	5 wt% MX-156	2830 ± 180	62 ± 3	74 ± 1	2.2 ± 0.1	1700 ± 150	Tough
D230	1 wt% MX-257	3215 ± 240	62 ± 2	82 ± 1	1.7 ± 0.1	1000 ± 150	Tough
D230	5 wt% MX-257	2670 ± 330	57 ± 1	75 ± 1	2.6 ± 0.1	2500 ± 200	Tough
D400	None	2556 ± 170	57 ± 4	68 ± 1	1.5 ± 0.2	760 ± 200	Tough

obtained from quasistatic tensile tests, listed in Table 36.2. The curve representing Eq. (36.1) follows the trend for the brittle group of data surprisingly well. The ballistic limit of the brittle resins is underpredicted by Eq. (36.1) by a consistent margin of about 0.5 normalized KE_{50} . Such a gap is not surprising because Eq. (36.1) predicts the critical impact velocity to initiate a cone crack, whereas the V_{50} test measures penetration of a witness foil behind the specimen by the projectile or an ejected fragment of the specimen. The gap of 0.5 normalized KE_{50} may represent the additional impact energy required to eject a cone section fragment from a specimen after initiating conical cracking. As shown in Fig. 36.7 and discussed above, radial cracking occurs prior to cone crack initiation, allowing conical fragments to dislodge relatively easily after forming. It is remarkable that the trend for brittle samples is well described by Eq. (36.1) with no adjustable parameters, since this equation was derived for ideal elastic, quasistatic Hertzian contact. Compton et al. [46] have presented finite element simulations suggesting that variations in contact radius due to plastic deformation cause dramatic deviations from the cone initiation threshold predicted by Eq. (36.1). Therefore, our result implies that plastic deformation does not influence the contact radius for brittle resins at failure velocity.

As seen in Fig. 36.9, data with $KE_{50} > 3$ are not a strong function of quasistatic K_{IC} , suggesting they may be best described by a relationship with the general form of Eq. (36.2). To test this hypothesis, we multiply Eq. (36.2) by an arbitrary constant A :

$$V_Y = \frac{3A\sigma_{Y,2}}{(\rho c)^{1/2}} \quad (36.3)$$

The blue dotted curve in Fig. 36.9 represents a fit to Eq. (36.3) using $A = 3.8$ and yield stress and Young's modulus values from quasistatic tensile tests of selected filled and unfilled resins in the tough group, listed in Table 36.2. In reality, stresses in the plastic zone ahead of impact are a combination of tensile and compressive, and thus the fit using tensile yield stress is an approximation. Use of measured compressive yield stress values (also included in Table 36.2) for Eq. (36.3) results in a similarly good fit to the data, using a value of $A = 3$ rather than 3.8.

The value of A was chosen simply to give a good fit to the experimental KE_{50} data for tough samples, but it may represent a combination of physical phenomena. First, as discussed above, Eq. (36.2) was derived for ceramic targets with high yield stress, in which the contact radius is determined by plastic deformation of the projectile prior to yield of the target at high velocities. In our system it is the target rather than the projectile that first deforms plastically; thus a portion the prefactor A in Eq. 36.3 may account for different contact geometry. Secondly, Eq. 36.2 was derived as an approximate limit for *initiation* of yield at the target front face, whereas the KE_{50} data are measurements of complete target failure characterized by ejection of fragments or the projectile from the specimen's back face. Hence, a portion of A may constitute the additional energy required for full target failure after initiating plasticity, analogous to the gap of 0.5 between Eq. 36.1 and KE_{50} of the brittle samples. Thirdly, it is well known that mechanical properties of glassy polymers are highly rate dependent [52]. Quasistatic yield stress and modulus values used to construct the blue curve in Fig. 36.9 were measured at a nominal strain rate of $3 \times 10^{-3} \text{ s}^{-1}$, while the ballistic impact events occur at effective strain rates between 10^4 and 10^5 s^{-1} . Therefore a significant portion of the prefactor A in Eq. 36.3 may account for the increase in yield stress over the quasistatic value due to the high rate of ballistic impact. The combination of these reasonable physical considerations, as well as the good agreement between Eq. 36.3 and KE_{50} of tough resins reported here, suggest that ballistic failure may be dominated by plastic yielding of the target for materials with fracture toughness above a certain threshold defined by the intersection of the two curves in Fig. 36.9.

Approximately five data points in Fig. 36.9 do not fit the trends described by Eqs. (36.1) or (36.3), comprising D230 modified with 0.5–2 wt% of either MX-125 or MX-156. These materials have relatively high quasistatic K_{IC} values between 1.1 and 2.0 $\text{MPa}\cdot\text{m}^{1/2}$, yet their KE_{50} is lower than that predicted by Eq. (36.3) for the high K_{IC} , plastic yield dominated regime. A possible explanation for these outliers is that the toughening effects of MX-125 and MX-156 have a greater rate dependence than that of MX-257, as suggested above in the analysis of Fig. 36.8. In this case high rate K_{IC} would be much less than quasistatic K_{IC} , shifting these data to the left where they may fall along the trend defined by the red dashed curve (Eq. 36.1). On the other hand MX-257 modified D230 behaves like a tough material with $KE_{50} \approx 3.5$ for all compositions from 0.5 to 9 wt%. This contrast is particularly striking when considering the case of D230 modified with 0.5 wt% MX-257 ($K_{IC} = 1.1 \text{ MPa}\cdot\text{m}^{1/2}$, $KE_{50} = 3.3$), which approximately fits both trends and is thus apparently near the transition point between brittle and tough regimes.

36.4 Conclusions

We have demonstrated that core-shell rubber (CSR) nanoparticle modifiers are capable in some cases of improving ballistic performance of amine-cured epoxy resins without significantly lowering T_g or stiffness. The CSR particles impart dramatic improvements to ballistic impact resistance of resins within a relatively narrow range of T_g between 60 and 110 °C, whereas resins above or below this T_g range show little ballistic improvement with addition of CSR particles. While brittle resins with low molecular weight between crosslinks tend to exhibit modestly increasing KE_{50} as a function of fracture toughness K_{IC} , a limiting value of about 3.5 normalized KE_{50} was found for tougher formulations, irrespective of measured quasistatic K_{IC} . These trends are well described by two different failure mechanisms: for brittle materials ballistic failure is dominated by the critical velocity for Hertzian cone crack initiation, while for tough materials ballistic limit is related to the critical velocity for target plastic yield at the impact site. These insights will inform the design of next generation adhesives and matrix materials for fiber-reinforced composites used in a variety of lightweight protective applications.

References

- Grossman, E., Gouzman, I.: Space environment effects on polymers in low earth orbit. *Nucl. Instrum. Methods Phys. Res. B* **208**, 48–57 (2003)
- Committee on Opportunities in Protection Materials Science Technology for Future Army Applications and National Research Council: Opportunities in Protection Materials Science and Technology for Future Army Applications. The National Academies Press, Washington (2011)
- Crawford, E., Lesser, A.J.: The effect of network architecture on the thermal and mechanical behavior of epoxy resins. *J. Polym. Sci. Polym. Phys.* **36**(8), 1371–1382 (1998)
- Naik, N.K., Shirao, P.: Composite structures under ballistic impact. *Compos. Struct.* **66**(1–4), 579–590 (2004)
- Carrillo, J.G., et al.: Ballistic performance of thermoplastic composite laminates made from aramid woven fabric and polypropylene matrix. *Polym. Test.* **31**(4), 512–519 (2012)
- Hsieh, T.H., et al.: The toughness of epoxy polymers and fibre composites modified with rubber microparticles and silica nanoparticles. *J. Mater. Sci.* **45**(5), 1193–1210 (2009)
- Sprengr, S.: Fiber-reinforced composites based on epoxy resins modified with elastomers and surface-modified silica nanoparticles. *J. Mater. Sci.* **49**(6), 2391–2402 (2013)
- David, N.V., Gao, X.L., Zheng, J.Q.: Ballistic resistant body armor: contemporary and prospective materials and related protection mechanisms. *Appl. Mech. Rev.* **62**(5), 050802 (2009)
- Naik, N.K., et al.: High strain rate mechanical behavior of epoxy under compressive loading: experimental and modeling studies. *Mater. Sci. Eng. A* **528**(3), 846–854 (2011)
- Knorr Jr., D.B., et al.: Glass transition dependence of ultrahigh strain rate response in amine cured epoxy resins. *Polymer* **53**(25), 5917–5923 (2012)
- Masser, K.A., et al.: Relating structure and chain dynamics to ballistic performance in transparent epoxy networks exhibiting nanometer scale heterogeneity. *Polymer* **58**, 96–106 (2015)
- Knorr, D.B., et al.: Overcoming the structural versus energy dissipation trade-off in highly crosslinked polymer networks: ultrahigh strain rate response in polydicyclopentadiene. *Compos. Sci. Technol.* **114**, 17–25 (2015)
- McGarry, F.J.: Building design with fibre reinforced materials. *Proc. R Soc. Lond. A Math. Phys. Sci.* **319**(1536), 59–68 (1970)
- Kinloch, A.J., et al.: Deformation and fracture behaviour of a rubber-toughened epoxy: 1. Microstructure and fracture studies. *Polymer* **24**, 1341–1354 (1983)
- Yee, A.F., Pearson, R.A.: Toughening mechanisms in elastomer-modified epoxies Part 1 mechanical studies. *J. Mater. Sci.* **21**, 2462–2474 (1986)
- Spanoudakis, J., Young, R.J.: Crack propagation in a glass particle-filled epoxy resin Part 1—effect of particle volume fraction and size. *J. Mater. Sci.* **19**, 473–486 (1984)
- Hsieh, T.H., et al.: The mechanisms and mechanics of the toughening of epoxy polymers modified with silica nanoparticles. *Polymer* **51**(26), 6284–6294 (2010)
- McGrath, L.M., et al.: Investigation of the thermal, mechanical, and fracture properties of alumina-epoxy composites. *Polymer* **49**(4), 999–1014 (2008)
- Sue, H.J., et al.: Optimization of mode-I fracture toughness of high-performance epoxies by using designed core-shell rubber particles. *Adv. Chem. Ser.* **233**, 259–291 (1993)
- Blanco, M., et al.: Thermoplastic-modified epoxy resins cured with different functionalities amine mixtures: morphology, thermal behavior, and mechanical properties. *J. Appl. Polym. Sci.* **114**(3), 1753–1760 (2009)
- Fischer, M.: Properties and failure of polymers with tailored distances between cross-links. *Adv. Polym. Sci.* **100**, 313–355 (1992)
- Garg, A.C., Mai, Y.W.: Failure mechanisms in toughened epoxy resins—a review. *Compos. Sci. Technol.* **31**(3), 179–223 (1988)
- Bagheri, R., Marouf, B.T., Pearson, R.A.: Rubber-toughened epoxies: a critical review. *Polym. Rev.* **49**(3), 201–225 (2009)
- Pearson, R.A., Yee, A.F.: Toughening mechanisms in elastomer-modified epoxies. Part 2—Microscopy studies. *J. Mater. Sci.* **21**, 2475–2488 (1986)
- Pearson, R.A., Yee, A.F.: Toughening mechanisms in elastomer-modified epoxies 3. The effect of cross-link density. *J. Mater. Sci.* **24**(7), 2571–2580 (1989)
- Dean, J.M., et al.: Micellar structure and mechanical properties of block copolymer-modified epoxies. *J. Polym. Sci. Polym. Phys.* **39**, 2996–3010 (2001)
- Liu, J., et al.: Strain rate effect on toughening of nano-sized PEP-PEO block copolymer modified epoxy. *Acta Mater.* **57**(9), 2691–2701 (2009)
- Liu, J., et al.: Nanocavitation in self-assembled amphiphilic block copolymer-modified epoxy. *Macromolecules* **41**, 7616–7624 (2008)
- Thompson, Z.J., et al.: Block copolymer toughened epoxy—role of crosslink density. *Macromolecules* **42**, 2333–2335 (2009)
- Sue, H.J., et al.: Fracture mechanisms in rigid core shell particle modified high performance epoxies. *Colloid Polym. Sci.* **274**(4), 342–349 (1996)
- Bagheri, R., Pearson, R.A.: Role of blend morphology in rubber-toughened polymers. *J. Mater. Sci.* **31**, 3945–3954 (1996)
- Lu, F., et al.: Toughening mechanisms in modified epoxy resins with different crosslink densities. *Polym. Bull.* **37**(3), 399–406 (1996)
- Huang, Y., Kinloch, A.J.: Modeling of the toughening mechanisms in rubber-modified epoxy polymers Part I. Finite element analysis studies. *J. Mater. Sci.* **27**, 2753–2762 (1992)
- Huang, Y., Kinloch, A.J.: Modelling of the toughening mechanisms in rubber-modified epoxy polymers Part II—A quantitative description of the microstructure-fracture property relationships. *J. Mater. Sci.* **27**, 2763–2769 (1992)
- Arias, M.L., Frontini, P.M., Williams, R.J.J.: Analysis of the damage zone around the crack tip for two rubber-modified epoxy matrices exhibiting different toughenability. *Polymer* **44**(5), 1537–1546 (2003)
- Aizpurua, B., et al.: Chemorheology and ultimate behavior of epoxy-amine mixtures modified with a liquid oligomer. *J. Appl. Polym. Sci.* **76**(8), 1269–1279 (2000)

37. Bradley, W.L., et al.: The synergistic effect of cross-link density and rubber additions on the fracture toughness of polymers. *Adv. Chem. Ser.* **233**, 317–334 (1993)
38. Raghavan, D., et al.: Strain rate dependence of fracture in a rubber-toughened epoxy system. *J. Adhes.* **78**(8), 723–739 (2002)
39. Cardwell, B.J., Yee, A.F.: Rate and temperature effects on the fracture toughness of a rubber-modified epoxy. *Polymer* **34**(8), 1695–1701 (1993)
40. Bain, E.D., et al.: Failure processes governing high-rate impact resistance of epoxy resins filled with core-shell rubber nanoparticles. *J. Mater. Sci.* **51**(5), 2347–2370 (2015)
41. US Department of Defense: V50 ballistic test for armor MIL-STD-662F (1997)
42. Bogoslovov, R.B., Roland, C.M., Gamache, R.M.: Impact-induced glass transition in elastomeric coatings. *Appl. Phys. Lett.* **90**(22), 221910 (2007)
43. Roland, C.M.: Mechanical behavior of rubber at high strain rates. *Rubber Chem. Technol.* **79**(3), 429–459 (2006)
44. Roland, C.M., Fragiadakis, D., Gamache, R.M.: Elastomer-steel laminate armor. *Compos. Struct.* **92**(5), 1059–1064 (2010)
45. Roland, C.M., et al.: Factors influencing the ballistic impact resistance of elastomer-coated metal substrates. *Philos. Mag.* **93**(5), 468–477 (2013)
46. Compton, B.G., Gamble, E.A., Zok, F.W.: Failure initiation during impact of metal spheres onto ceramic targets. *Int. J. Impact Eng.* **55**, 11–23 (2013)
47. Seagraves, A.N., Radovitzky, R.A.: An analytical theory for radial crack propagation: application to spherical indentation. *J. Appl. Mech.* **80**, 041018 (2013)
48. Lawn, B.R.: Indentation of ceramics with spheres: a century after Hertz. *J. Am. Ceram. Soc.* **81**, 1977–1994 (1998)
49. Sherman, D., Brandon, D.G.: The ballistic failure mechanisms and sequence in semi-infinite supported alumina tiles. *J. Mater. Res.* **12**, 1335–1343 (1997)
50. Sherman, D.: Impact failure mechanisms in alumina tiles on finite thickness support and the effect of confinement. *Int. J. Impact Eng.* **24**, 313–328 (2000)
51. Qian, J.Y., et al.: The role of dispersed phase morphology on toughening of epoxies. *Polymer* **38**(1), 21–30 (1997)
52. Iwamoto, T., Nagai, T., Sawa, T.: Experimental and computational investigations on strain rate sensitivity and deformation behavior of bulk materials made of epoxy resin structural adhesive. *Int. J. Solids Struct.* **47**, 175–185 (2010)